3D Macroporous Graphene Frameworks for Supercapacitors with High Energy and Power Densities

Bong Gill Choi,[†,⊥] MinHo Yang,[†,⊥] Won Hi Hong,[‡] Jang Wook Choi,[§,*] and Yun Suk Huh[†,*]

[†]Division of Materials Science, Korea Basic Science Institute, Daejeon, 305-333, Republic of Korea, [‡]Department of Chemical & Biomolecular Engineering (BK21 Program), KAIST, Daejeon 305-701, Republic of Korea, and [§]Graduate School of EEWS (WCU) and KAIST Institute NanoCentury, KAIST, Daejeon 305-701, Republic of Korea. [⊥]These authors contributed equally to this work.

ABSTRACT

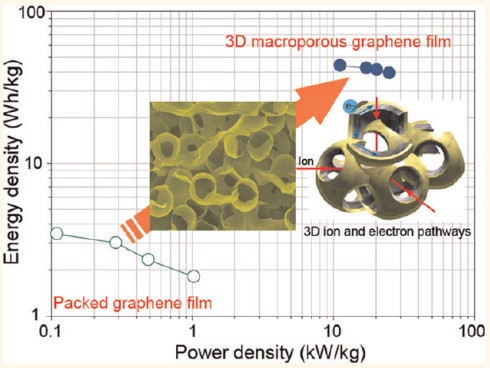

In order to develop energy storage devices with high power and energy densities, electrodes should hold well-defined pathways for efficient ionic and electronic transport. Herein, we demonstrate high-performance supercapacitors by building a three-dimensional (3D) macroporous structure that consists of chemically modified graphene (CMG). These 3D macroporous electrodes, namely, embossed-CMG (e-CMG) films, were fabricated by using polystyrene colloidal particles as a sacrificial template. Furthermore, for further capacitance boost, a thin layer of MnO_2 was additionally deposited onto e-CMG. The porous graphene structure with a large surface area facilitates fast ionic transport within the electrode while preserving decent electronic conductivity and thus endows MnO_2/e-CMG composite electrodes with excellent electrochemical properties such as a specific capacitance of 389 F/g at 1 A/g and 97.7% capacitance retention upon a current increase to 35 A/g. Moreover, when the MnO_2/e-CMG composite electrode was asymmetrically assembled with an e-CMG electrode, the assembled full cell shows remarkable cell performance: energy density of 44 Wh/kg, power density of 25 kW/kg, and excellent cycle life.

KEYWORDS: porous material · graphene · composites · ion transport · energy storage

The energy and power densities of energy storage devices should be improved significantly to meet the growing power supply demand of a variety of applications such as cordless electric tools, hybrid electric vehicles, day–night storage, and industrial energy management.[1−3] In this context, supercapacitors are considered to be very attractive energy storage devices, as they have high power density and cycling stability.[4−7] However, supercapacitors are still not capable of delivering high energy densities comparable to those of lithium ion batteries, and this drawback restricts the use of supercapacitors mainly to high-power applications such as emergency power supplies, hybrid bus, and portable power tools. The energy density (E) of supercapacitors depends on the cell potential (V) and capacitance (C), based on $E = 1/2(CV^2)$.[5] These two parameters are determined mainly by electrodes, and therefore, previous attempts at increasing the capacitance of supercapacitors have dealt extensively with various electrode materials including carbonaceous materials, conducting polymers, transition metal oxides, and their composites.[8−11] More recently, the development of supercapacitors has focused on the use of graphene, due to its excellent electrical and mechanical properties, chemical stability, high specific surface area up to 2675 m^2/g, and feasibility for large-scale production (especially the chemically modified graphenes (CMGs)).[12−14] Graphene-based symmetric supercapacitor devices show a large electrical double layer capacitance (around 100–200 F/g using aqueous and organic electrolytes).[15−17] Higher capacitances (200–550 F/g) can be obtained by combining graphenes with other pseudocapacitive materials, *e.g.*, RuO_2, MnO_2, and polyaniline.[18−20] Despite these significant efforts, the energy densities of these supercapacitors remain substandard (<20 Wh/kg) for many important applications. Recently, several groups have demonstrated that integrating a battery-type pseudocapacitive electrode (as an energy source) and a capacitive electrode (as a power source) in the same cell to form an asymmetric supercapacitor improves the energy and power densities, because of an increased voltage window up to ~2 V.[21−23] For example, Cheng *et al.*

* Address correspondence to jangwookchoi@kaist.ac.kr; yshuh@kbsi.re.kr.

Received for review January 23, 2012 and accepted April 13, 2012.

Published online April 23, 2012
10.1021/nn3003345

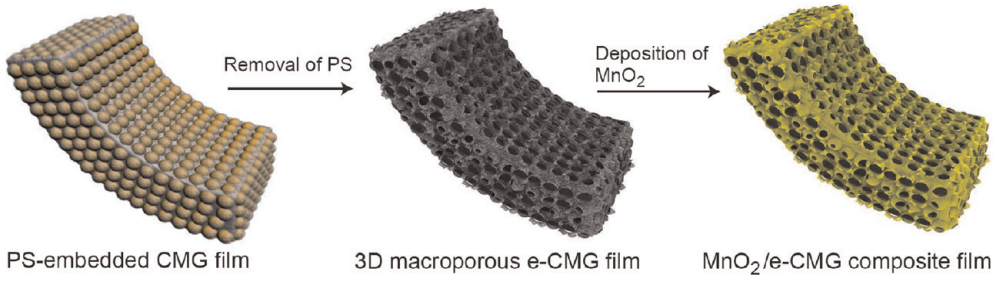

Scheme 1. Schematic illustrating a procedure to fabricate 3D macroporous films through an embossing process using PS templates for e-CMG film as well as a subsequent deposition process of MnO_2 for MnO_2/e-CMG film.

reported a maximum energy density of 30.4 Wh/kg and power density of 5 kW/kg using graphene//MnO_2/graphene hybrid cells.[23] Although considerable research effort has been devoted to enhancing device performance so far, the inefficient ionic and electronic transport in pseudocapacitive-based electrodes has led to capacitance fading over cycling or at high rates, causing a major bottleneck in the performance in various aspects.[24,25] Obviously, the structure and morphology of the electrode materials are very critical for resolving these limitations of ionic and electronic transport, and thus achieving supercapacitors that can combine high power and energy densities, long cycle life, and high rate capability.

Ionic and electronic transport kinetics lie at the heart of energy storage and conversion systems.[26] Recent reports and reviews have described electrode construction consisting of three-dimensional (3D) interpenetrating structures that could provide a good solution to the issue of poor ionic and electronic transport in electrode materials, thereby resulting in high-performance devices.[27,28] In particular, 3D macroporous frameworks have been produced by integrating graphene-based materials with polymers and self-assembly. Although these 3D structures show potential for use as capacitive electrodes, those electrical double-layer capacitors exhibited relatively low energy densities due to the intrinsic limitation of the electrostatic surface charging mechanism.[9,29,30] To address the inferior energy densities of EDLCs, one promising approach would be the construction of heterogeneous structures based on more than one component, which can provide the synergistic effect of individual constituents on both power and energy densities.[4,5,8] Most of works on graphene-based nanocomposites have been achieved by incorporating guest nanoparticles onto 2D graphene sheets. However, those structures suffer from graphene aggregation, which causes inferior ionic accessibility and thus modest improvement in the cell performance.[12] Obviously, the disordered nanocomposite films containing the aggregated graphene make it difficult for ions to gain access to the electrode surfaces and thus become a scientific and technical challenge.

In the present paper, we employ a well-known replicating and embossing technique to fabricate 3D macroporous CMG films by using polystyrene (PS) colloidal particles as sacrificial templates.[31,32] The resulting macroporous embossed CMG (e-CMG) films have a large surface area, a 3D porous network interconnected with CMG sheets, and excellent mechanical integrity. The unique electrode structure not only boosted ion and electron movement in electrochemical processes but also enabled the porous e-CMG films to serve as a 3D skeleton for combining the e-CMG films with metal oxides such as MnO_2. As an effort to utilize these 3D macroporous e-CMG films for energy storage devices with high levels of power and energy densities, asymmetric supercapacitors were assembled in a way that e-CMG and MnO_2/e-CMG films function as negative and positive electrodes, respectively. Although macroporous graphene structures have been developed through various procedures,[21,29,30] the templating process described in this study is much simpler, and macroporous graphene structures based on the templating method have never been reported for energy storage applications.

RESULTS AND DISCUSSION

The e-CMG films were prepared in two steps: fabrication of free-standing PS/CMG films by vacuum filtration of a mixed aqueous colloidal suspension of CMG and PS (2.0 μm PS spheres), followed by removal of the PS to generate 3D macropores (Scheme 1). This filtration process is suitable for macroscopic assembly of CMG sheets into "paper-like" bulk materials with high electrical conductivity and mechanical flexibility.[33] We fabricated well-ordered free-standing PS/CMG films by filtration, by first separately preparing a negatively charged CMG colloidal and a positively charged PS suspension.[34,35] A mixture of CMG and a PS suspension was dispersed in solution under controlled pH (=2), where the two compounds had the same surface charges (zeta potential values of $+13 \pm 2.4$ mV for CMG and $+68 \pm 5.6$ mV for PS). When the pH was raised to 6, CMGs (zeta potential = -29 ± 3.7 mV) and PS spheres (zeta potential = $+51 \pm 2.5$ mV) were assembled due to the electrostatic interactions and hydrophobic characteristics between them, and these were subsequently integrated into PS/CMG composite films through a filtering process. The SEM images

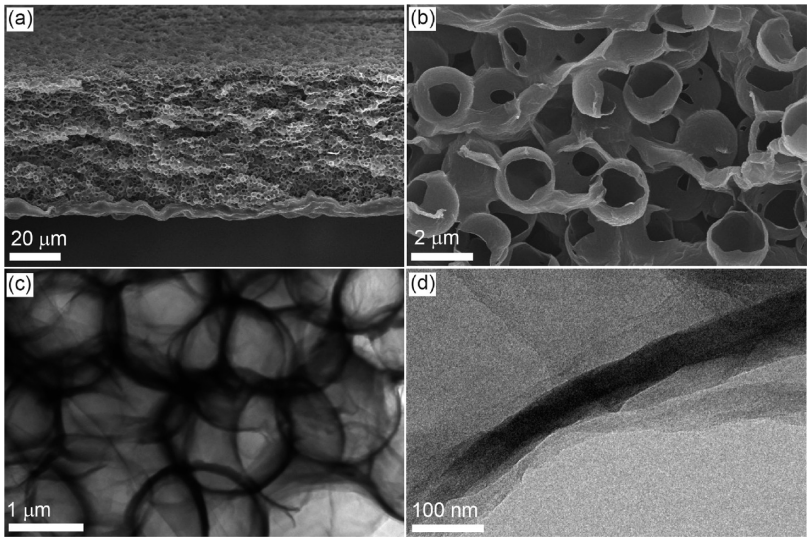

Figure 1. (a) Low-magnified and (b) high-magnified cross-sectional SEM images of e-CMG film. (c and d) TEM images at different magnifications of e-CMG film.

clearly showed that CMG-wrapped PS nanoparticles were packed into multilayers, forming crinkles and rough textures (Supporting Information, Figure S1). It is noteworthy that the dimensions of both CMG ($0.87 \pm 0.48\ \mu$m) and PS spheres ($\sim 2\ \mu$m) as well as the intrinsic flexibility of graphene are appropriate enough to hold the curvature and thus the overall porous structure. The PS particles in the PS/CMG composite film were selectively removed using toluene, leaving behind an open porous structure (Figure 1a and b). The porous structure did not collapse after the removal of the PS template because of the interconnected nature of the multilayered CMG walls in the assembled 3D structure (Figure 1c and d). The mechanical strength of graphene, the pore size ($\sim 2\ \mu$m), and the weak volatility of toluene at room temperature synergistically help preserve the porous structure even after solvent evaporation. The well-defined interconnecting pore networks of the e-CMG films also showed a high electrical conductivity (1204 S/m).

We were able to incorporate MnO_2 into the e-CMG film by dipping the films into a solution of 0.1 M $NaMnO_4$/0.1 M Na_2SO_4 for neutral pH and at various dipping times (10−60 min).[36] MnO_2 was incorporated into the 3D porous structures based on controlled self-limiting deposition.[36,37] After the deposition of MnO_2, the retention of the 3D macroporous structure was confirmed by high-angle annular dark-field scanning TEM (HAADF-STEM), as shown in Figure 2a. In particular, energy-dispersive X-ray spectroscopic (EDS) elemental maps of C, O, and Mn (Figure 2a) clearly verified the homogeneous coating of amorphous MnO_2 throughout the 3D macroporous frameworks. In addition, a nanoscale conformal coating of amorphous MnO_2 on the CMG surface was observed in the high-resolution HAADF image of Figure 2b, in which the protruding CMG sheets were entirely coated with MnO_2 layers (coating thickness of 20−30 nm). The complete coverage of the MnO_2 layers was further confirmed by X-ray photoelectron spectroscopy (XPS) of the MnO_2/e-CMG film. When the Mn 2p spectrum was analyzed (Figure 2c), it was observed that two characteristic peaks of Mn $2p_{1/2}$ and Mn $2p_{3/2}$ were located at 654.1 and 642.4 eV, respectively, which are in good agreement with previous reported data.[37] No MnO_2 peaks were detected in the XRD patterns for the composite film, indicating that the manganese oxide layers were amorphous (Supporting Information, Figure S2), which is consistent with previous reports based on redox-deposited MnO_2 on carbon materials.[36,37] The CMG and MnO_2/CMG films prepared without using PS nanoparticles were tested as reference samples under identical conditions. Due to the absence of template for pore generation, these films had highly packed structures rather than porous structures (Supporting Information, Figure S3). The characterization of top surfaces and cross sections gives more detailed effects of the porous structure on the deposition of MnO_2 layers. In the case of MnO_2/e-CMG (Supporting Information, Figure S4b), the MnO_2 deposition was uniform over the entire film cross-section. By contrast, in the case of MnO_2/CMG (Supporting Information, Figure S4d), the MnO_2 deposition was more concentrated toward the top surface. Apparently, the uniform deposition for MnO_2/e-CMG is attributed to the well-defined porous structure that allows Mn precursor ions to gain access onto the graphene surfaces even deep inside the films during the Mn deposition. The top-view SEM image of the MnO_2/CMG film (Supporting Information, Figure S5) also supports the concentrated MnO_2 deposition on the top sample surfaces, as the deposition buries the morphology of intrinsic graphene. Overall, the porous structure contributes to the uniform deposition of

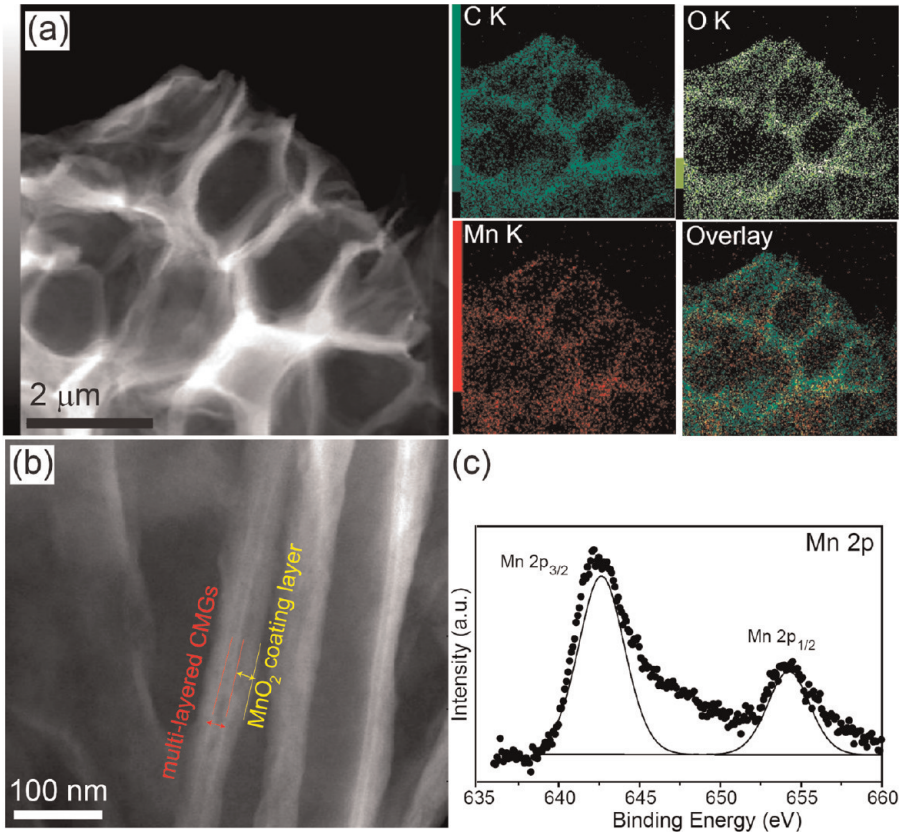

Figure 2. (a) HADDF-STEM image and EDS mapping of C, O, Mn, and overlay elements on a segment of MnO_2/e-CMG film. (b) High-resolution HADDF-STEM image of MnO_2/e-CMG film. (c) Representative Mn 2p XPS spectra of MnO_2/e-CMG film.

MnO_2 layers over the entire graphene films. In addition, the construction of the porous structure dramatically increased the surface area: N_2 sorption−desorption measurements give surface areas of 18.52, 13.59, 194.20, and 142.01 m^2/g for CMG, MnO_2/CMG, e-CMG, and MnO_2/e-CMG, respectively (Supporting Information, Table S1). Overall, this straightforward approach is highly desirable for constructing 3D heterostructured materials to be used as capacitive electrodes because active materials with high capacitances can be conformally coated on the 3D porous backbone.

The electrochemical performance of e-CMG and MnO_2/e-CMG films with large accessible surface areas and pore structures was evaluated as capacitive electrodes using a conventional three-electrode system with Ag/AgCl as the reference electrode and Pt wire as the counter electrode in an aqueous electrolyte solution of 1 M Na_2SO_4. For reference samples, the CMG and MnO_2/CMG films were tested under identical conditions. As shown in the cyclic voltammetry (CV) curves in Figure 3a, symmetric and horizontal CV curves were observed for both e-CMG and CMG films, indicating ideal electrical double layer capacitive behavior. When MnO_2 was deposited, higher current densities were observed for the MnO_2/e-CMG and MnO_2/CMG films than those for the analogues without MnO_2 layers, which suggested that the introduction of MnO_2 contributes to the increase in the capacitance. As expected, higher current densities were found for the 3D transport pathway-based e-CMG and MnO_2/e-CMG films than those for the CMG-based counterparts.

The capacitive performance was further investigated with galvanostatic charge/discharge cycling experiments (Figure 3b). On the basis of the discharging curve line, the specific capacitance of the e-CMG film was calculated to be 202 F/g at 1 A/g, which was two times higher than that of the CMG film (93 F/g). In addition, the specific capacitance significantly increased as the MnO_2 deposition time was increased up to 60 min (Figure 3c). This result was ascribed to the faradic contribution of MnO_2 to the CMG-based electrical double layer capacitance. The macroporous MnO_2/e-CMG film, produced with a dipping time of 60 min, reached a maximum value of 389 F/g at 1 A/g, which was approximately three times higher than those of the MnO_2/CMG film (137 F/g) and was also higher than those of other reported MnO_2/graphene materials including needle-like MnO_2/graphene composite (216 F/g at 0.15 A/g),[19] MnO_2/graphene composite paper (256 F/g at 0.5 A/g),[38] and MnO_2/graphene textiles (315 F/g at 2 mV/s).[21] More importantly, at a high rate of 35 A/g, the MnO_2/e-CMG film maintained 97.7% retention of its initial specific capacitance measured at 0.5 A/g (Figure 3d). This value was similar to

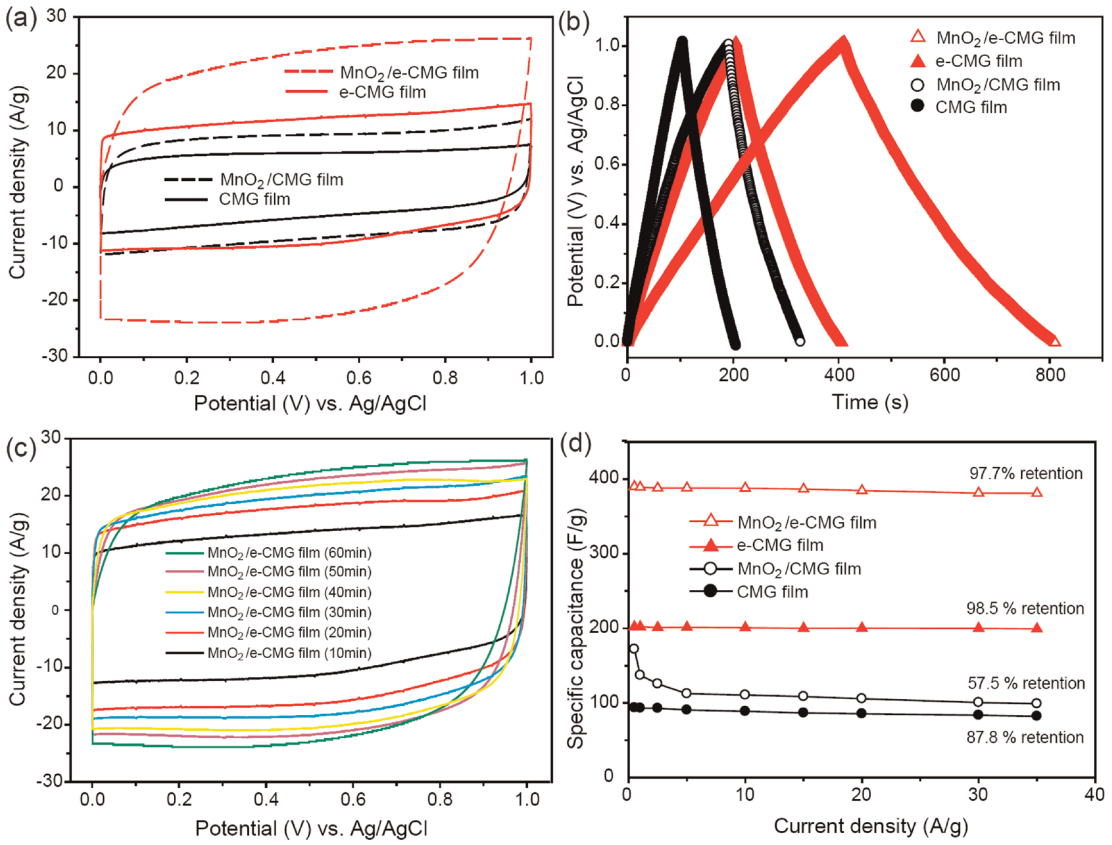

Figure 3. (a) CV curves measured at a scan rate of 50 mV/s for CMG, MnO_2/CMG (60 min dipping), e-CMG, and MnO_2/e-CMG (60 min dipping) films. (b) Galvanostatic charge–discharge curves measured at a constant current density of 1 A/g for CMG, MnO_2/CMG, e-CMG, and MnO_2/e-CMG films in 1 M Na_2SO_4. (c) CV curves obtained from MnO_2/e-CMG films at a scan rate of 50 mV/s as a function of dipping time. (d) Dependences of the specific capacitances of CMG, MnO_2/CMG (60 min dipping), e-CMG, and MnO_2/e-CMG (60 min dipping) films on various current densities ranging from 0.5 to 35 A/g for charge/discharge behavior.

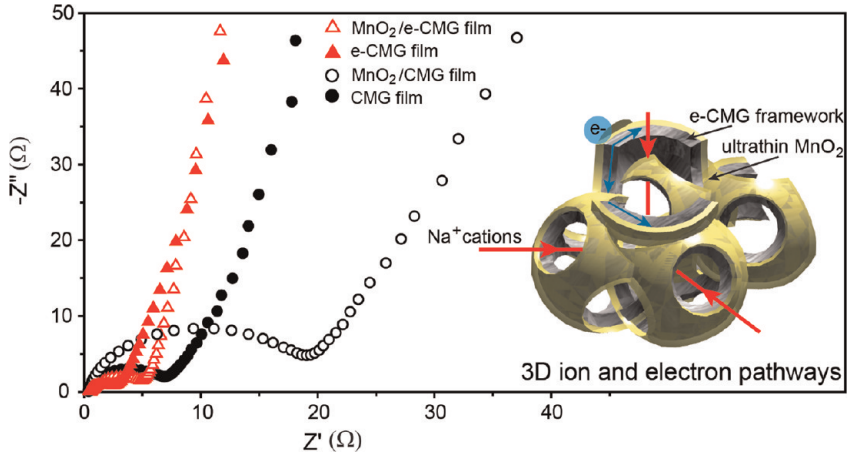

Figure 4. Nyquist plots for CMG, MnO_2/CMG (60 min dipping), e-CMG, and MnO_2/e-CMG (60 min dipping) films. Inset image illustrates 3D ionic and electronic transport pathways in the MnO_2/e-CMG electrode.

that of the e-CMG film (98.5% retention). In contrast, although the CMG film retained 87.8% of its specific capacitance at 35 A/g, the MnO_2/CMG film retained only 57.5% at the same current density. The improved rate capability of the MnO_2/e-CMG film, compared to the MnO_2/CMG film, indicates again that the 3D macroporous structure allows for effective ion migration into the active sites, thereby generating reversible capacitive behavior even at high charging/discharging rates.

Further understanding of the fast ion diffusion in macroporous films was obtained by conducting ac

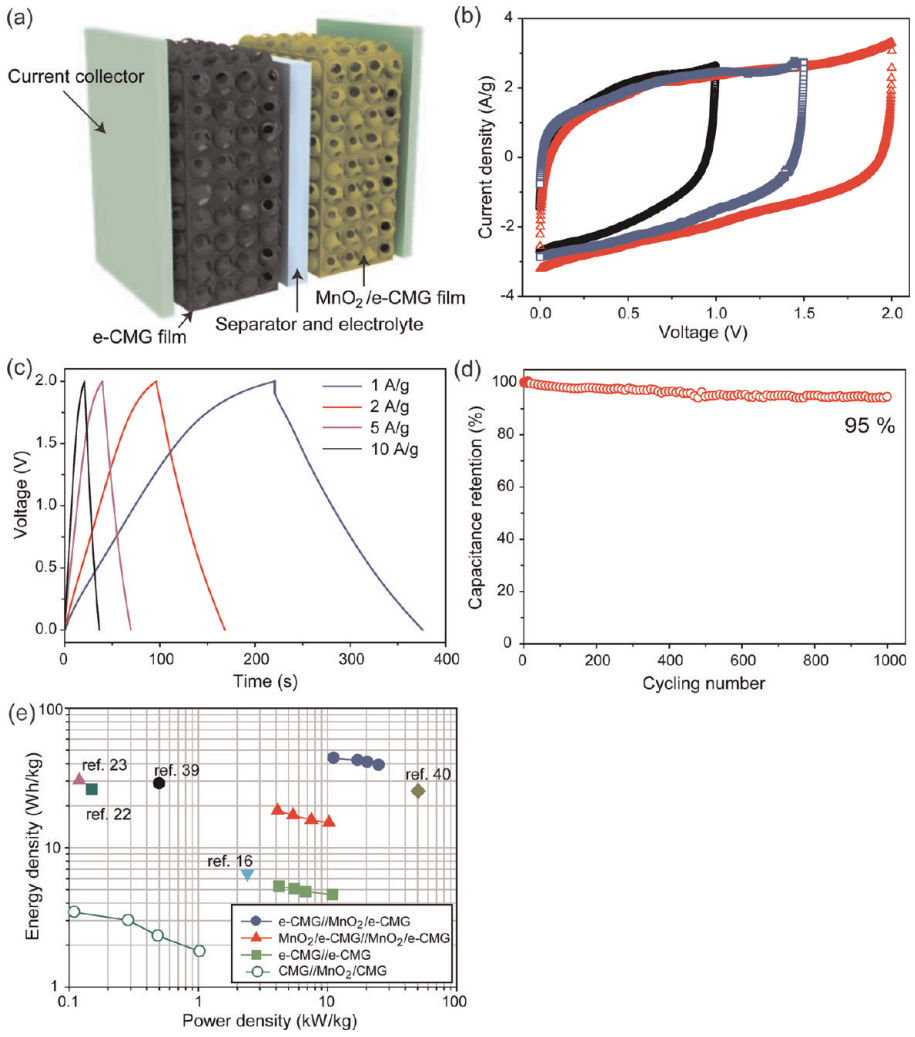

Figure 5. (a) Schematic diagram of e-CMG//MnO_2/e-CMG-based asymmetric supercapacitor device. (b) CV curves obtained from the asymmetric supercapacitor with different cell voltages of 1, 1.5, and 2.0 V at a scan rate of 50 mV/s. (c) Galvanostatic charge/discharge curves of asymmetric supercapacitor measured at different current densities of 1, 2, 5, and 10 A/g. (d) Long-term cycling stability of the asymmetric supercapacitor at a constant current density of 1 A/g over 1000 cycles. (e) Ragone plot of the symmetric (e-CMG//e-CMG and MnO_2/e-CMG//MnO_2/e-CMG) and asymmetric (CMG//MnO_2/CMG and e-CMG//MnO_2/e-CMG) supercapacitors compared with data in other literature.

impedance measurements at a frequency range of 100 kHz to 0.01 Hz. The Nyquist plots for all the samples are shown in Figure 4. According to the equivalent circuit,[33] the charge transfer resistance (R_{CT}) was calculated to be 1.7, 3.4, 5.6, and 15.8 Ω for e-CMG, MnO_2/e-CMG, CMG, and MnO_2/CMG, respectively. The decreasing R_{CT} trend from the CMG-based samples to the e-CMG-based counterparts should be associated with the increased contact area at the electrode–electrolyte interface. Again, the porous nature of the e-CMG samples plays a critical role along this direction. At the low frequency region, a more vertical straight line was evident for the porous film than for packed film, which indicates the faster ion diffusion behavior of the porous film. More detailed analyses were carried out by fitting the impedance data to an equivalent circuit consisting of a series of a resistor and a capacitor. From the plotting, the relaxation time constant, a representative of diffusion kinetics, can be obtained, and its value was conspicuously varied depending on the presence of porosity in the electrode: e-CMG exhibited a relaxation time constant of 101.0 ms, whereas CMG exhibited 1265.8 ms. The shorter relaxation time of e-CMG must stem from the well-defined porous structure that facilitates the efficient ionic diffusion. Detailed analyses are described in the Supporting Information. This result clearly implies that the electrolyte ions move more easily into the 3D porous channels compared to the 2D packed structure. Consequently, this macroporous network allowed efficient and fast ion diffusion between three-dimensionally connected MnO_2 and electrolytes, while the interconnected CMG sheets provided continuous electron pathways through the MnO_2 and served as a double-layer capacitor (inset scheme image of Figure 4). On the basis of these electrochemical results, we speculate

that the macroscopic pore structure and hybrid capacitive characteristics of the MnO_2/e-CMG films enhanced the electrochemical performance of supercapacitor devices.

An asymmetric supercapacitor device was prepared by assembling an e-CMG film as a negative electrode and a MnO_2/e-CMG film as a positive electrode. These were sandwiched within nitrocellulose films and immersed in 1 M Na_2SO_4 solution (Figure 5a). We ensured the cell voltage of the asymmetric device by performing a pre-experiment of CV measurements in a three-electrode cell separately with e-CMG and MnO_2/e-CMG films (Supporting Information, Figure S7). A stable potential window was observed in the range from −1.0 to 0.2 V for e-CMG and from 0.0 to 1.0 V for MnO_2/e-CMG. These results suggest that asymmetric supercapacitor devices can be operated up to 2.0 V. Indeed, the cell voltage of this hybrid device can be expanded from 1.0 to 2.0 V, as shown in Figure 5b. In addition, this device operated in a stable voltage window of 2.0 V even at a high current density of 10 A/g (Figure 5c). This result was ascribed to the fast surface electrosorption of Na^+ cations as well as the fast and reversible faradic process that occurred between Na^+ cations and MnO_2. The cycling stability of the asymmetric supercapacitor device was tested at a constant current density of 1 A/g for 1000 cycles. As shown in Figure 5d, 95% of the initial capacitance was retained, indicating good long-term stability of the asymmetric supercapacitor based on the macroporous films. The galvanostatic charge/discharge curves were used to evaluate the power (*P*) and energy (*E*) densities of our supercapacitor devices (detailed information is described in the Experimental Section). Figure 5e shows a Ragone plot of the corresponding specific *E versus P* values. The maximum energy density of 44 Wh/kg (with a power density of 11.2 kW/kg) and power density of 25 kW/kg (with energy density of 39.1 Wh/kg) were achieved by our asymmetric supercapacitors with an operating potential of 2.0 V. These values are higher than those of symmetric e-CMG//e-CMG and MnO_2/e-CMG//MnO_2/e-CMG supercapacitors, a CMG//MnO_2/CMG asymmetric supercapacitor, and other devices reported previously.[16,22,23,39,40] This improved performance can be understood as an effect of the 3D ion and electron pathways on capacitive behavior and the wide cell voltage of 2 V.

CONCLUSION

In conclusion, we demonstrated that the rational design and fabrication of 3D macroporous e-CMG films through a simple embossing process provide rapid pathways for ionic and electronic transport, thus providing tremendous potential for energy storage applications. In particular, MnO_2/e-CMG prepared by simple deposition of MnO_2 onto macropores delivered a 2-fold higher specific capacitance than that for e-CMG. More importantly, the integration of e-CMG and MnO_2/e-CMG films into an asymmetric supercapacitor device enabled the combination of high energy density, high rate capability, and long cycling life. Finally, the electrode structure and fabrication method described in this study is simple and should thus be readily applicable to other graphene-based energy storage and conversion applications in which efficient ionic and electronic transport is critical.

EXPERIMENTAL SECTION

Preparation of 3D Macroporous e-CMG and MnO_2/e-CMG Films. To integrate CMG sheets into a macroscopic assembly, graphene oxides (GOs) were initially prepared by the modified Hummers method.[34] As-prepared GO suspensions were dispersed in water (0.05 wt % dispersion) by a sonication process. The homogeneous GO solution (5 mL) was chemically reduced by sequentially adding 35 μL of ammonia solution (28 wt % in water, Junsei) and 5 μL of hydrazine solution (35 wt % in water, Aldrich). Then, the GO solution was located in a water bath at 95 °C for 1 h. The resultant solution of the negatively charged CMGs was collected by washing and filtering with water and ethanol several times.[35] The PS solution was prepared by dispersing PS particles (10 wt %, 2 μm mean particle size, Aldrich) in deionized water at pH 2. Both the CMG and PS solutions (95:5 in weight ratio) were also mixed at pH 2. Throughout the entire fabrication procedures, the pH control is critical for producing the final continuous PS/CMG films. At pH 2, both PS and CMG were positively charged and were thus hardly agglomerated. By contrast, when both components were oppositely charged, they easily agglomerated and did not thus form continuous films. The PS/CMG films were produced by filtering the mixed solution through anodizc membrane filters (25 mm in diameter, 0.2 μm pore size, Whatman) by vacuum suction. During this filtration, the pH of the solution was adjusted to 6 by adding 1 M sodium hydroxide (NaOH) solution. The pH change was to make both components oppositely charged (CMG: negative, PS: positive) and thus stimulate the electrostatic interactions between both components, leading to the uniform distribution of PS particles in the CMG films. The free-standing PS/CMG films were obtained by peeling them off from the filter membrane. The final e-CMG films were obtained by removing the PS colloidal particles with toluene exposure. The control samples, CMG and MnO_2/CMG, were prepared by the same procedures, but in the absence of PS particles. The MnO_2/e-CMG films were fabricated by dipping the films in a solution of 0.1 M $NaMnO_4$/0.1 M Na_2SO_4 at a neutral pH at room temperature (RT). MnO_2 was deposited into pore structure by a self-limiting reaction with deposition times of 10−60 min. The composite films were rinsed in water several times and dried at 60 °C for 24 h. The resultant CMG and e-CMG films have the same mass, but different film thicknesses of ~8 μm for CMG and ~55 μm for e-CMG films. The weight (~10 mg for each electrode) of the samples was measured as freestanding films using a semimicro balance (Sartorius Genius, ME235S) with a readability of 0.01 mg.

Fabrication of Asymmetric Supercapacitor Devices. The e-CMG and MnO_2/e-CMG films were attached on the Al foils as both electrodes and current collectors. The asymmetric supercapacitor devices were prepared by assembling e-CMG film as the negative electrode and MnO_2/e-CMG film as the positive electrode separated by the aqueous electrolyte soaked separator (nitrocellulose film). The as-obtained supercapacitor devices were dried at RT before the devices were measured.

Structure Characterization. TEM and HAADF-STEM images were collected on an E.M. 912 Ω energy-filtering TEM (JEM-2200 FS). The elemental mapping in the scanning TEM was operated with a probe focused to 0.2 nm and camera length of 20 cm. SEM images were obtained using a field emission scanning electron microscope (S-4800). XPS data were obtained using a VG Multilab 2000 (Thermo VG Scientific) with a monochromatic Mg Kα X-ray source ($h\nu$ = 1253.6 eV) under 10^{-7} Torr vacuum analysis chamber. The high-resolution scans of C and low-resolution survey scans were analyzed for each sample at, at least, two separated locations.

The X-ray diffraction (XRD) data were obtained on a Rigaku D/max IIIC (3 kW) with a θ/θ goniometer equipped with a Cu Kα radiation generator. The diffraction angle of the diffractograms was in the range $2\theta = 5-80°$. Electrical conductivities of our porous films were measured by using the standard four-point probe technique (Loresta-GP, Mitsubishi Chemical) as in other previous reports.[34] The samples were cut with a razor into rectangular strips of 1 × 1 cm^2. The thicknesses of the samples were measured from cross-sectional SEM images. All of the conductivity data were obtained at room temperature and within an error range of ±1%.

Electrochemical Characterization. Electrochemical experiments were carried out using a three-electrode system for the obtained e-CMG or MnO_2/e-CMG films and two-electrode configuration for supercapacitor devices. In measurements with a three-electrode system, the transferred e-CMG or MnO_2/e-CMG films on Al foil as working electrode were investigated with a Ag/AgCl reference electrode and a Pt counter electrode in an electrolyte solution of 1 M Na_2SO_4. The electrochemical characteristics were evaluated by cyclic voltammetry using a CHI 760D electrochemical workstation (CH Instruments) and galvanostatic charge/discharge using a Solartron 1287 at RT. The electrochemical impedance spectroscopy measurements were performed over a frequency range from 10^5 to 10^{-2} Hz at the amplitude of the sinusoidal voltage of 10 mV and RT using a Solartron 1260 impedance/gain-phase analyzer. The cycle life tests were conducted by galvanostatic charge/discharge measurements with a constant current density of 1 A/g for 1000 cycles. The power and energy densities were calculated by using the following equations:[8]

$$E = 1/2C_T(\Delta V)^2, \quad P = (\Delta V)^2/4RM$$

where C_T, ΔV, R, and M are the total capacitance of the entire device, the potential window of discharge, the internal resistance from *IR* drop, and the total mass of both electrodes, respectively. The internal resistances (*IR* drop) were determined from the voltage drop at the beginning of the galvanostatic discharge curves. The total capacitance (C_T) was calculated by using the following equation:

$$C_T = I/(\Delta V/\Delta t)$$

where I and $\Delta V/\Delta t$ are the applied current density and the discharge slope after *IR* drop, respectively. All of the values including the current densities were normalized with respect to the combined weight of both electrodes.

Conflict of Interest: The authors declare no competing financial interest.

Acknowledgment. We acknowledge the financial support by the National Research Foundation of Korea Grant funded by the Korean Government (MEST, NRF-2010-C1AAA001-0029018) and by KBSI grant T32413. J.W.C. acknowledges the World Class University Program (R-31-2008-000-10055-0) for financial support. We would like to thank Dr. Young Boo Lee at KBSI for taking HADDF-STEM images.

Supporting Information Available: Cross-sectional SEM image of PS-embedded CMG film; XRD patterns for e-CMG and MnO_2/e-CMG films; SEM image of CMG film; SEM images and EDS mapping (C, Mn) for surface and cross-section of MnO_2/e-CMG and MnO_2/CMG; high-resolution SEM image of MnO_2/CMG film (top view); real part and imaginary part of the capacitance with the frequencies for CMG and e-CMG films; comparative CV curves obtained from e-CMG and MnO_2/e-CMG films, respectively. This material is available free of charge *via* the Internet at http://pubs.acs.org.

REFERENCES AND NOTES

1. Miller, J. R.; Burke, A. F. Electrochemical Capacitors: Challenges and Opportunities for Real-World Applications. *Electrochem. Soc. Interface* **2008**, *17*, 53–57.
2. Liu, C.; Li, F.; Ma, L.-P.; Cheng, H.-M. Advanced Materials for Energy Storage. *Adv. Mater.* **2010**, *22*, E28–E62.
3. Armaroli, N.; Balzani, V. Towards an Electricity-Powered World. *Energy Environ. Sci* **2011**, *4*, 3193–3222.
4. Zaho, X.; Sánchez, B. M.; Dobson, P. J.; Grant, P. S. The Role of Nanomaterials in Redox-Based Supercapacitors for Next Generation Energy Storage Devices. *Nanoscale* **2011**, *3*, 839–855.
5. Hall, P. J.; Mirzaeian, M.; Fletcher, S. I.; Sillars, F. B.; Rennie, A. J. R.; Shitta-Bey, G. O.; Wilson, G.; Cruden, A.; Carter., R. Energy Storage in Electrochemical Capacitors: Designing Functional Materials to Improve Performance. *Energy Environ. Sci.* **2010**, *3*, 1238–1251.
6. Zhu, Y.; Murali, S.; Stoller, M. D.; Ganesh, K. J.; Cai, W.; Ferreira, P. J.; Pirkle, A.; Wallace, R. M.; Cychosz, K. A.; Thommes, M.; *et al.* Carbon-Based Supercapacitors Produced by Activation of Graphene. *Science* **2011**, *332*, 1537–1541.
7. Jeong, H. M.; Lee, J. W.; Shin, W. H.; Choi, Y. J.; Shin, H. J.; Kang, J. K.; Choi, J. W. Nitrogen-Doped Graphene for High-Performance Ultracapacitors and the Importance of Nitrogen-Doped Sites at Basal Planes. *Nano Lett.* **2011**, *11*, 2472–2477.
8. Zhang, L. L.; Zhao, X. S. Carbon-Based Materials as Supercapacitor Electrodes. *Chem. Soc. Rev.* **2009**, *38*, 2520–2531.
9. Simon, P.; Gogotsi, Y. Materials for Electrochemical Capacitors. *Nat. Mater.* **2008**, *7*, 845–854.
10. Lang, X.; Hirata, A.; Fujita, T.; Chen, M. Nanoporous Metal/Oxide Hybrid Electrodes for Electrochemical Supercapacitors. *Nat. Nanotechnol.* **2011**, *6*, 232–236.
11. Nyholm, L.; Nyström, G.; Mihranyan, A.; Strømme, M. Toward Flexible Polymer and Paper-Based Energy Storage Devices. *Adv. Mater.* **2011**, *23*, 3751–3769.
12. Sun, Y.; Wu, Q.; Shi, G. Graphene Based New Energy Materials. *Energy Environ. Sci.* **2011**, *4*, 1113–1132.
13. Gao, W.; Singh, N.; Song, L.; Liu, Z.; Reddy, A. L. M.; Ci, L.; Vajtai, R.; Zhang, Q.; Wei, B.; Ajayan, P. M. Direct Laser Writing of Micro-Supercapacitors on Hydrated Graphite Oxide Films. *Nat. Nanotechnol.* **2011**, *6*, 496–500.
14. Miller, J. R.; Outlaw, R. A.; Holloway, B. C. Graphene Double-Layer Capacitor with ac Line-Filtering Performance. *Science* **2010**, *329*, 1637–1639.
15. Stoller, M. D.; Park, S.; Zhu, Y.; An, J.; Ruoff, R. S. Graphene-Based Ultracapacitors. *Nano Lett.* **2008**, *8*, 3498–3502.
16. Kim, T. Y.; Lee, H. W.; Stoller, M.; Dreyer, D. R.; Bielawski, C. W.; Ruoff, R. S.; Suh, K. S. High-Performance Supercapacitors Based on Poly(ionic liquid)-Modified Graphene Electrodes. *ACS Nano* **2011**, *5*, 436–442.
17. Zhu, Y.; Murali, S.; Cai, W.; Li, X.; Suk, J. W.; Potts, J. R.; Ruoff, R. S. Graphene and Graphene Oxide: Synthesis, Properties, and Applications. *Adv. Mater.* **2010**, *22*, 3906–3924.
18. Wu, Z.-S.; Wang, D.-W.; Ren, W.; Zhao, J.; Zhou, G.; Li, F.; Cheng, H.-M. Anchoring Hydrous RuO_2 on Graphene Sheets for High-Performance Electrochemical Capacitors. *Adv. Funct. Mater.* **2010**, *20*, 3595–3602.
19. Chen, S.; Zhu, J.; Wu, X.; Han, Q.; Wang, X. Graphene Oxide-MnO_2 Nanocomposites for Supercapacitors. *ACS Nano* **2010**, *4*, 2822–2830.
20. Wu, Q.; Xu, Y.; Yao, Z.; Liu, A.; Shi, G. Supercapacitors Based on Flexible Graphene/Polyaniline Nanofiber Composite Films. *ACS Nano* **2010**, *4*, 1963–1970.
21. Yu, G.; Hu, L.; Vosgueritchian, M.; Wang, H.; Xie, X.; McDonough, J. R.; Cui, X.; Cui, Y.; Bao, Z. Solution-Processed Graphene/MnO_2 Nanostructured Textiles for High-Performance Electrochemical Capacitors. *Nano Lett.* **2011**, *11*, 2905–2911.
22. Zhang, J.; Jiang, J.; Li, H.; Zhao, X. S. A High-Performance Asymmetric Supercapacitor Fabricated with Graphene-Based Electrodes. *Energy Environ. Sci.* **2011**, *4*, 4009–4015.
23. Wu, Z.-S.; Ren, W.; Wang, D.-W.; Li, F.; Liu, B.; Cheng, H.-M. High-Energy MnO_2 Nanowire/Graphene and Graphene Asymmetric Electrochemical Capacitors. *ACS Nano* **2010**, *4*, 5835–5842.

24. Wei, W.; Cui, X.; Chen, W.; Ivey, D. G. Manganese Oxide-Based Materials as Electrochemical Supercapacitor Electrodes. *Chem. Soc. Rev.* **2011**, *40*, 1697–1721.
25. Bélanger, D.; Brousse, T.; Long, J. W. Manganese Oxides: Battery Materials Make the Leap to Electrochemical Capacitors. *Electrochem. Soc. Interface* **2008**, *17*, 49–52.
26. Maier, J. Nanoionics: Ion Transport and Electrochemical Storage in Confined Systems. *Nat. Mater.* **2005**, *4*, 805–815.
27. Liu, R.; Duay, J.; Lee, S. B. Heterogeneous Nanostructured Electrode Materials for Electrochemical Energy Storage. *Chem. Commun.* **2011**, *47*, 1384–1404.
28. Rolison, D. R.; Long, J. W.; Lytle, J. C.; Fischer, A. E.; Rhodes, C. P.; McEvoy, T. M.; Bourg, M. E.; Lubers, A. M. Multifunctional 3D Nanoarchitectures for Energy Storage and Conversion. *Chem. Soc. Rev.* **2009**, *38*, 226–252.
29. Lee, S. H.; Kim, H. W.; Hwang, J. O.; Lee, W. J.; Kwon, J.; Bielawski, C. W.; Ruoff, R. S.; Kim, S. O. Three-Dimensional Self-Assembly of Graphene Oxide Platelets into Mechanically Flexible Macroporous Carbon Films. *Angew. Chem., Int. Ed.* **2010**, *49*, 10084–10088.
30. Xu, Y.; Sheng, K.; Li, C.; Shi, G. Self-Assembled Graphene Hydrogel *via* a One-Step Hydrothermal Process. *ACS Nano* **2010**, *4*, 4324–4330.
31. Das, R. K.; Liu, B.; Reynolds, J. R.; Rinzler, A. G. Engineered Macroporosity in Single-Wall Carbon Nanotube Films. *Nano Lett.* **2009**, *9*, 677–683.
32. Hong, J.; Char, K.; Kim, B.-S. Hollow Capsules of Reduced Graphene Oxide Nanosheets Assembled on a Sacrificial Colloidal Particle. *J. Phys. Chem. Lett.* **2010**, *1*, 3442–3445.
33. Choi, B. G.; Hong, J.; Hong, W. H.; Hammond, P. T.; Park, H. Facilitated Ion Transport in All-Solid-State Flexible Supercapacitors. *ACS Nano* **2011**, *5*, 7205–7213.
34. Hummers, W. S.; Offeman, R. E. Preparation of Graphitic Oxide. *J. Am. Chem. Soc.* **1958**, *80*, 1339.
35. Li, D.; Müller, M. B.; Gilje, S.; Kaner, R. B.; Wallace, G. G. Processable Aqueous Dispersions of Graphene Nanosheets. *Nat. Nanotechnol* **2008**, *3*, 101–105.
36. Fischer, A. E.; Pettigrew, K. A.; Rolison, D. R.; Stroud, R. M.; Long, J. W. Incorporation of Homogeneous, Nanoscale MnO_2 within Ultraporous Carbon Structures *via* Self-Limiting Electroless Deposition: Implications for Electrochemical Capacitors. *Nano Lett.* **2007**, *7*, 281–286.
37. Lee, S. W.; Kim, J.; Chen, S.; Hammond, P. T.; Shao-Horn, Y. Carbon Nanotube/Manganese Oxide Ultrathin Film Electrodes for Electrochemical Capacitors. *ACS Nano* **2010**, *4*, 3889–3896.
38. Li, Z.; Mi, Y.; Liu, X.; Liu, S.; Yang, S.; Wang, J. Flexible Graphene/MnO_2 Composite Papers for Supercapacitor Electrodes. *J. Mater. Chem.* **2011**, *21*, 14706–14711.
39. Hong, M. S.; Lee, S. H.; Kim, S. W. Use of KCl Aqueous Electrolyte for 2 V Manganese Oxide/Activated Carbon Hybrid Capacitor. *Electrochem. Solid-State Lett.* **2002**, *5*, A227–A230.
40. Chen, P.-C.; Shen, G.; Shi, Y.; Chen, H.; Zhou, C. Preparation and Characterization of Flexible Asymmetric Supercapacitors Based on Transition-Metal-Oxide Nanowire/Single Walled Carbon Nanotube Hybrid Thin-Film Electrodes. *ACS Nano* **2010**, *4*, 4403–4411.